#### **Research Article**

Zhoukun He, Jie Su, Xiaowei Zhu\*, Yue Li, Libo Yang, Xudong Zhang, Qi Jiang, and Xiaorong Lan\*

# Integrated structure-function design of 3D-printed porous polydimethylsiloxane for superhydrophobic engineering

https://doi.org/10.1515/rams-2024-0074 received August 15, 2024; accepted November 25, 2024

Abstract: Three-dimensional (3D) printing technology can be used to fabricate layer-by-layer regular porous polydimethylsiloxane (PDMS) structures with excellent superhydrophobic ability and mechanical stability. However, for engineering applications, the design must consider the structure and superhydrophobicity of the resulting material. In this study, we propose an approach to regulate the mechanical properties of PDMS by adjusting the layered pattern, such as by changing filament orientation with 30°, 45°, and 90° angle steps and using staggered structures with a half-shifted spacing. A finite element analysis was conducted to investigate how the layered pattern influenced the tensile and compressive properties. The results reveal that a layered, staggered design can modulate the compressive properties of the porous PDMS, particularly the ratio between the compressive moduli of the sample without and with staggered structures could reach as high as 686% when the layering angle is 0°/90°. The tensile properties are better regulated by the filament angle rather than by the staggered design and improve as the raster angle of the filaments increases. This occurs when the upper and lower filaments tend toward orthogonality. Thus, the required layered pattern can be selected, enabling the integrated design of mechanical properties and function in 3Dprinted porous PDMS.

**Keywords:** mechanical properties, 3D printing, PDMS, superhydrophobic, wettability

#### 1 Introduction

Superhydrophobicity is a unique type of wettability categorized by the contact angle of a spherical (or nearspherical) water droplet on a solid surface. In particular, superhydrophobic surfaces have a water contact angle (WCA) of >150° [1–3]. Flora and fauna, such as lotus leaves [4], water striders [5,6], dragonflies [7], and butterflies [8,9], possess inherent hydrophobicity [10-12]. The superhydrophobic surface wettability of various surfaces primarily depends on their low surface energy chemistry and unique micro/ nanostructures. Polydimethylsiloxane (PDMS) is a widely used material owing to its low surface energy [13,14] and good physical [15,16], chemical [17,18], and biomedical properties [19–21]. Previous methods, such as impregnation [11,22], spraying [23], chemical/physical etching [12,24], the sol-gel method [25], and the template method [26], have been employed to establish structural features of PDMS and its composites at the micro/nanoscales. These typical methods often involve many deficiencies, such as complex multi-step processing [27], use of solvent [22], or low precision in controlling the micro/nanostructures [24,28]. To achieve special surface wettability, such as anisotropy surface wettability or superhydrophobicity, techniques including UV lithography and femtosecond laser etching have often been adopted to form structures with asymmetric geometric character, such as fibers or grooves [29,30]. The formed structures can be widely applied according to their excellent properties, such as antifouling [31–36], waterproof protection [37], selective

**Zhoukun He, Jie Su:** School of Mechanical Engineering, Chengdu University, Chengdu, 610106, China; Institute for Advanced Study, Research Center of Composites & Surface and Interface Engineering, Chengdu University, Chengdu, 610106, China

**Yue Li, Libo Yang, Xudong Zhang:** School of Civil Engineering, Henan University of Technology, Zhengzhou, 450001, China

**Qi Jiang:** Sichuan Highland Engineering Design Consulting Co., Ltd, Chengdu, 610106, China

<sup>\*</sup> Corresponding author: Xiaowei Zhu, School of Civil Engineering, Henan University of Technology, Zhengzhou, 450001, China, e-mail: zhuxiaowei1989@126.com

<sup>\*</sup> Corresponding author: Xiaorong Lan, Luzhou Key Laboratory of Oral & Maxillofacial Reconstruction and Regeneration, The Affiliated Stomatological Hospital, Southwest Medical University, Luzhou, 646000, China; Basic Medicine Research Innovation Center for Cardiometabolic Diseases, Ministry of Education, Southwest Medical University, Luzhou, 646000, China; Institute of Stomatology, Southwest Medical University, Luzhou, 646000, China, e-mail: xiaoronglancdm@163.com

pattern printing [38], self-cleaning [39], liquid transfer [40], fog collection [41], and oil/water separation [42–44].

However, simultaneously achieving superhydrophobicity and good mechanical stability is challenging, and the fabrication of robust superhydrophobic materials with micro/nanostructures remains difficult. Recently, three-dimensional (3D) printing technologies have attracted attention in micro/nanostructure construction owing to certain advantages, including their flexible design and fabrication of highly complex structures for various applications, such as wound healing [45,46], heart valves [47], self-healing [48], microfluidics [49,50], and scaffolds [51,52]. Among these technologies, direct-write 3D printing can be used to prepare complex structures of different materials by designing an "ink" formulation and controlling the 3D printing process [53–55]. In our previous work, the final surface wettability and physical structure of the PDMS "ink" filament could be well controlled via the regulation of the 3D printing parameters, such as filament diameter or filament spacing, to obtain a regular porous PDMS material with excellent superhydrophobic ability and mechanical stability [53,55,56]. Adjusting the 3D printing parameters of the porous PDMS structure not only modulated its superhydrophobicity but also significantly impacted its mechanical properties. However, the optimal approach to regulate its mechanical properties while ensuring excellent superhydrophobic properties for its engineering application remains to be discovered. To date, limited studies have reported an integrated structure-function design of porous PDMS materials with excellent superhydrophobic ability and mechanical stability *via* 3D printing.

In this study, we extended preliminary experiments to regulate the mechanical properties, such as compressive and tensile properties, of superhydrophobic PDMS by designing layered and staggered structures and varying the filament angles without changing the superhydrophobic properties (that is, without modifying the filament diameter and spacing) [54]. The findings of this article will provide guidance for the physical structural design and preparation of mechanically stable, superhydrophobic regular PDMS materials by 3D printing. Moreover, this work can be used to further guide integrated structure—function design for applications in diverse fields, such as artificial skin and bioprosthetic heart valve materials in biomedicine and in energy and electronics applications.

#### 2 Methods

# 2.1 Fabrication of superhydrophobic PDMS using 3D printing

In this study, the *x*–*y* plane and *z*-direction were defined as the in-plane and height direction of the 3D-printed PDMS, respectively (Figure 1a). The customized high-viscosity

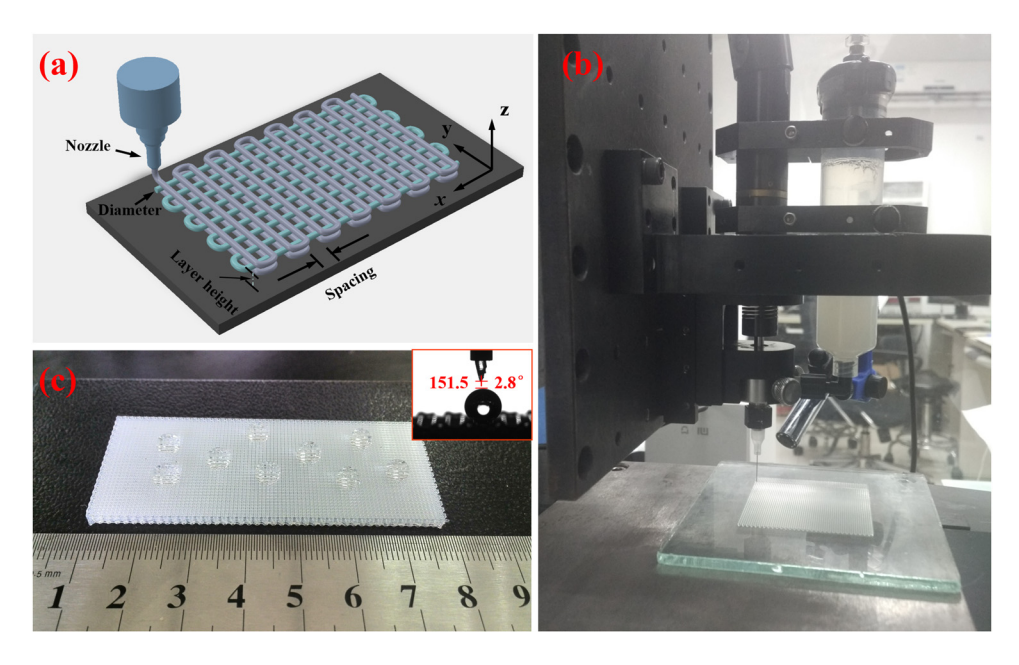


**Figure 1:** 3D printing of porous PDMS with a cross-hatched structure. (a) Schematic representation of the extruded filaments written on the substrates with the tooling path. (b) Fabrication of porous PDMS on the 3D printing platform. (c) PDMS foam sample with superhydrophobicity fabricated by 3D printing. The insert image is the profile of water droplets (5 μL) on the porous PDMS surface, with a WCA of approximately 151.5°.

PDMS ink was extruded through the nozzle of the 3D printing (direct-ink writing) system in the form of filaments [53]. The filaments were printed layer by layer according to the planned lay-down patterns at the corresponding printing speed to form a porous cross-hatched structure (Figure 1b). The 3D-printed structure was then cured and molded by placing it in an oven at 125°C for 24 h. Finally, the sample was peeled off from the substrate for further characterization. The PDMS surface had a filament diameter and filament spacing of 0.37 and 0.8 mm, respectively. It had four layers with 90° angle steps between two successive layers. When water droplets were placed onto the porous PDMS surface, they remained spherical, indicating that the surface showed good superhydrophobicity, with a WCA of approximately 151.5° (Figure 1c).

### 2.2 Design of the 3D-printed porous structure

Based on our previous work [57] and the classical Gibson-Ashby model for porous materials [58], the porosity  $(\varphi)$  of the 3D-printed PDMS sample had a direct impact on its mechanical properties, shown in Eq. (1). As the material porosity  $\varphi$  increased, its compressive or tensile modulus  $(E^*)$  gradually decreased.

$$\frac{E^*}{E_{\rm S}} = C \left(\frac{\rho^*}{\rho_{\rm S}}\right)^n = C(1-\phi)^n,\tag{1}$$

where  $E_{\rm S}$  and  $E^*$  are the modulus of elasticity of the solid and 3D-printed porous PDMS, respectively; C and n are the fitting coefficients; and  $\rho_{\rm S}$  and  $\rho^*$  are the density of the solid and 3D-printed porous PDMS, respectively [55].

Particularly,  $\varphi$  was correlated with the diameter (d), center-to-center spacing of the filaments (l), and height of the adjacent printed layers (h). According to the geometry of the porous PDMS fabricated by 3D printing, the solid volume  $V_1$  of the model was extracted by the software and then divided by the volume V (length × width × height) of the rectangular model. Finally, the model porosity  $\varphi$  of the PDMS sample was calculated using the formula  $\varphi = 1 - V_1/V$ . The results are theoretical and presented in Table 1.

As previously reported [53], the superhydrophobicity of 3D-printed porous PDMS was optimal when the filament diameter and spacing were 0.37 and 0.8 mm, respectively (Figure 1c). Therefore, we set the filament diameter d to 0.37 mm. Because the superhydrophobicity of the porous PDMS fabricated by 3D printing was primarily controlled by the top-layer structures of the porous PDMS [54], this study focused on the integrated structure and mechanical property design of the porous PDMS fabricated by 3D printing for superhydrophobic engineering. Even if the 3D-printed PDMS foams had the same porosity (same values for filament diameter, filament spacing, and layer height), the mechanical properties could still be regulated by adjusting the layer pattern (e.g., filament orientation and staggered structure) [59,60]. To demonstrate the universality of our strategy for modulating the mechanical properties, such as compressive and tensile, through the

Table 1: Model design parameters for the 3D-printed PDMS

Model number	Filament diameter (d) (mm)	Filament spacing (/) (mm)	Raster angle	Porosity ( $\varphi$ ) (%)
0/30-0.6	0.37	0.6	0°/30°/60°/90°	34.4
0/45-0.6			0°/45°/90°/135°	34.4
0/90-0.6			0°/90°/180°/270°	34.4
0/30-0.8		8.0	0°/30°/60°/90°	48.5
0/45-0.8			0°/45°/90°/135°	48.5
0/90-0.8			0°/90°/180°/270°	48.5
0/30-1.0		1.0	0°/30°/60°/90°	57.8
0/45-1.0			0°/45°/90°/135°	57.8
0/90-1.0			0°/90°/180°/270°	57.8
S-0/30-0.6	0.37	0.6	0°/30°/60°/90°	34.4
S-0/45-0.6			0°/45°/90°/135°	34.4
S-0/90-0.6			0°/90°/180°/270°	34.4
S-0/30-0.8		8.0	0°/30°/60°/90°	48.5
S-0/45-0.8			0°/45°/90°/135°	48.5
S-0/90-0.8			0°/90°/180°/270°	48.5
S-0/30-1.0		1.0	0°/30°/60°/90°	57.8
S-0/45-1.0			0°/45°/90°/135°	57.8
S-0/90-1.0			0°/90°/180°/270°	57.8

design of specific layered patterns, the filament spacing parameters were adjusted to 0.6, 0.8, and 1.0 mm. The raster angles were adjusted with 30° (0°/30°/60°/90° for four layers), 45° (0°/45°/90°/135° for four layers), and 90° (0°/90°/180°/270°) angle steps for a typical and gradual change of the intersection angle between two successive layers. The working parameters are shown in Table 1.

The superhydrophobic properties of the porous PDMS fabricated by 3D printing were primarily related to the filament spacing and diameter of the top layer [53,54]. Therefore, the mechanical properties were regulated by adjusting the lay-down patterns, and the spacing and diameter of the filaments remained unchanged. The architectures were designed by plotting filaments with angle steps of 30°, 45°, and 90° between two sequential layers, denoted 0/30, 0/45, and 0/90 configurations [61], respectively (Figure 2a–c). For the staggered pattern, every other layer was shifted orthogonally to the filament direction by half the spacing relative to the previous, yielding cross-hatched structures, labeled S-0/30, S-0/45, and S-0/90 configurations, respectively (Figure 2d–f). Notably,

the pore architecture depended on the filament orientation and layer stagger. For example, a filament deposition angle of 90° created quadrangular pores (Figure 2c and f), whereas angles of 30° or 45° generated polygonal pores (Figure 2a, b, d, and e).

#### 2.3 Finite element (FE) analysis models

For porous PDMS, compression and tension are the two most common mechanical stress states; thus, this study used these two stress models to evaluate the relationship between layer parameters and the mechanical performance of the porous PDMS fabricated by 3D printing. To further reveal the mechanism of strain and internal stress distribution in the 3D-printed PDMS with a cross-hatched structure under compressive or tensile load, the design models mentioned in Section 2.1 were created using FE analysis in ABAQUS. The PDMS filaments were cylindrical

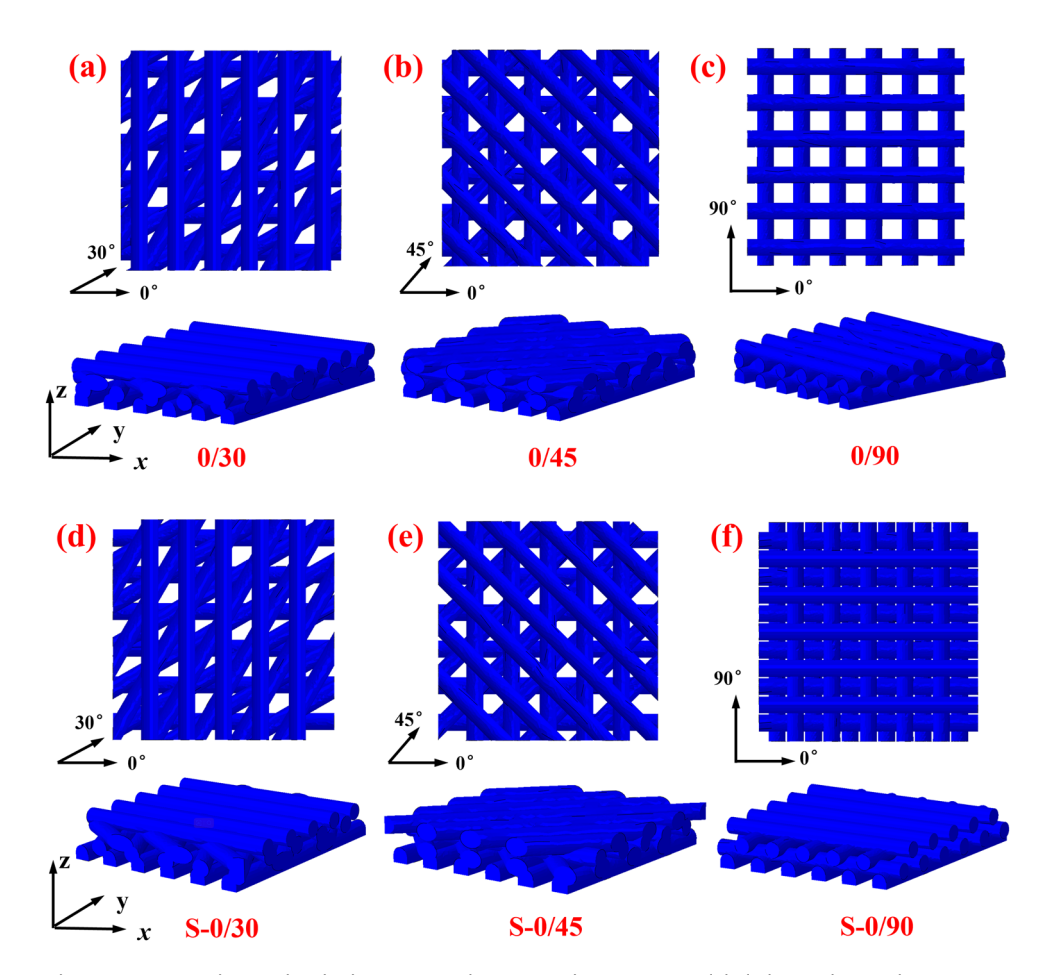


**Figure 2:** 3D-printed porous PDMS with cross-hatched structures. These printed patterns were labeled according to the 3D printing angle of the two successive layers: (a) 0/30, (b) 0/45, and (c) 0/90 configurations and (d) 0/30 (S-0/30), (e) 0/45 (S-0/45), and (f) 0/90 (S-0/90) shifted patterns.

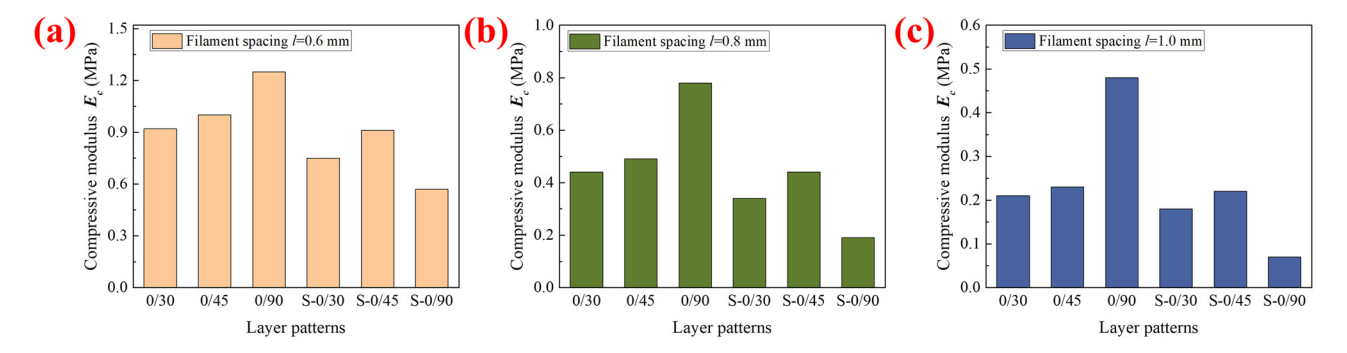


Figure 3: Effect of layered configurations on the  $E_c$  of porous PDMS fabricated by 3D printing with filament spacings of (a) 0.6, (b) 0.8, and (c) 1.0 mm.

apart from those of the first layer, and a total of four layers were constituted with six filaments per layer (Figure 2). The upper layer of the cylindrical filaments was rotationally stacked at a set angle with respect to the neighboring lower layer. Since the value of the print layer height parameter was smaller than the diameter of the PDMS filament, there was an overlapping region between the upper and lower print layers. The overlap area of the top and bottom layers was smoothed by a Boolean operation, and the porous PDMS model was treated as a single entity [55]. Free boundary conditions were imposed on these models. To study the compressive and tensile properties of the porous PDMS, we applied displacement loads in the zand y directions of these models, respectively. In addition, the mechanical properties of the porous PDMS fabricated by 3D printing were analyzed using the Mooney-Rivlin model [55,62], as expressed by the following equation:

$$U = C_{10}(I_1 - 3) + C_{01}(I_2 - 3) + \frac{1}{D_1}(J - 1)^2,$$
 (2)

where U is the strain energy of the materials,  $C_{10}$  and  $C_{01}$  are the fitted material coefficients,  $D_1$  is the compressibility of the material,  $I_1$  and  $I_2$  are the first and second invariants of the strain bias, respectively, and J is the elastic volume ratio [55]. Based on the constitutive model, the measured compressive nominal stress–strain data of the PDMS cylinder, with a diameter and height of 29.5 and 12.5 mm, respectively, have been modeled with the relevant parameters  $C_{10}$ ,  $C_{01}$ , and  $D_1$  [55]. These three fitted parameters, which were accessed by the analysis program in the FE software ABAQUS following our previous publication [55], were 0.203741993, 0.08319049733, and 0.177210526, respectively.

In addition, due to the superelastic characteristics of PDMS materials, these 3D-printed foams had a large mechanical deformation capacity in both compression and tensile

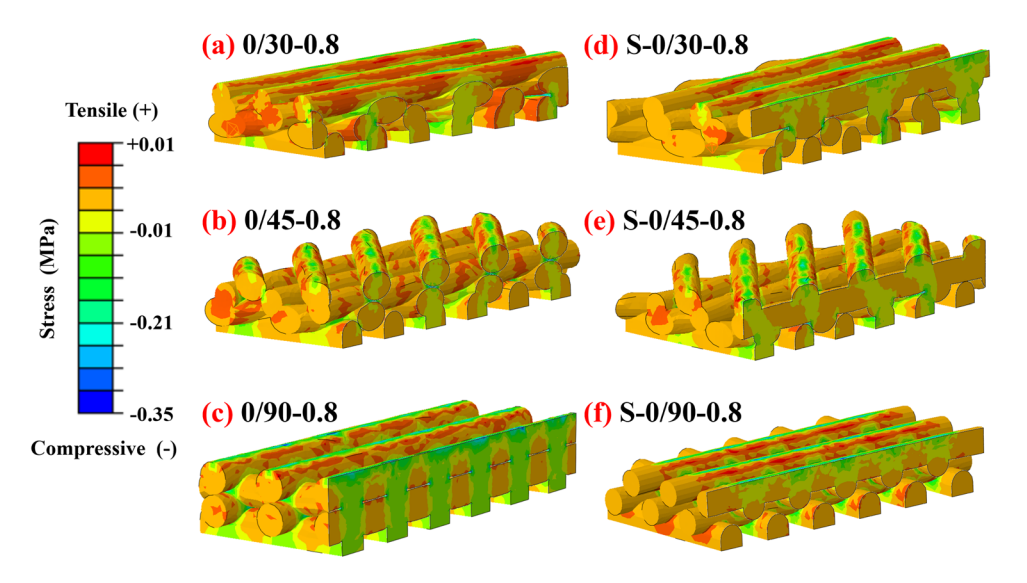


Figure 4: Stress distribution graphs in the x-z section of the models at 10% compressive strain: (a) 0/30-0.8, (b) 0/45-0.8, (c) 0/90-0.8, (d) S-0/30-0.8, (e) S-0/45-0.8, and (f) S-0/90-0.8.

6 — Zhoukun He et al. DE GRUYTER

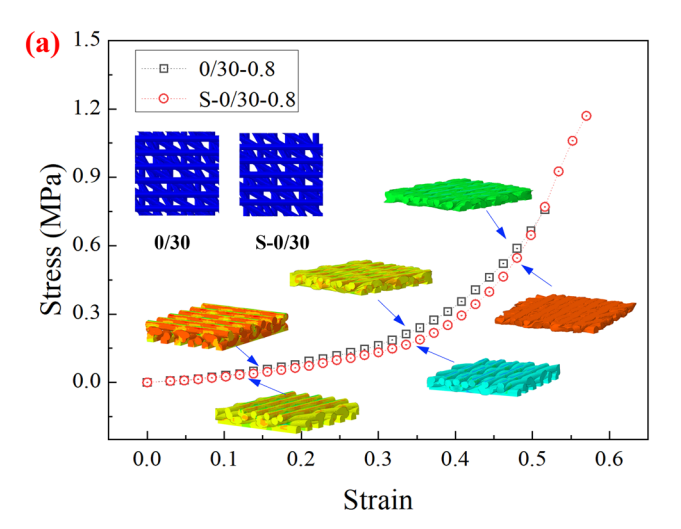
directions, which was sufficient to meet the engineering design requirements. The compression and tension properties can be found in the following section.

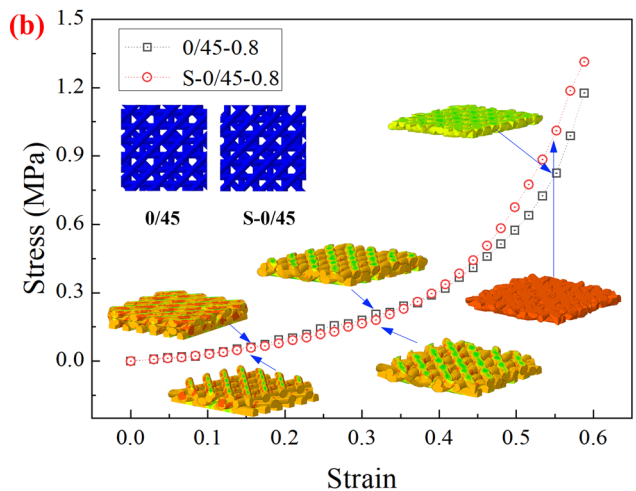
#### 3 Results and discussion

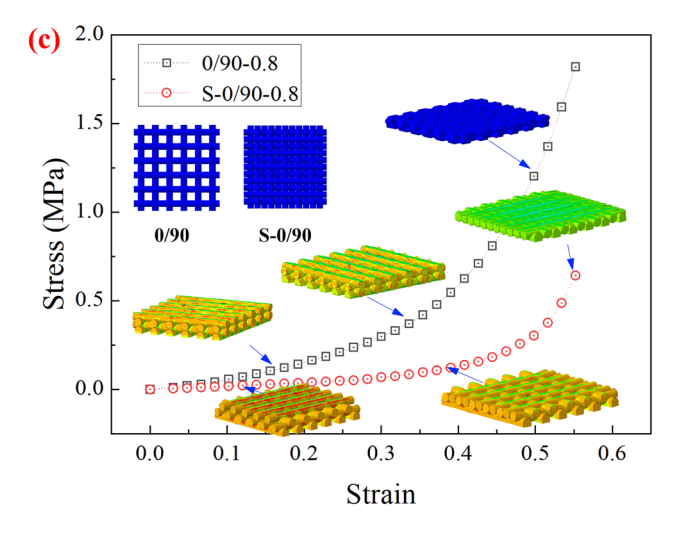
# 3.1 Effect of layered patterns on the compressive properties of 3D-printed PDMS

Figure 3 shows the z-axis compressive modulus  $E_{\rm c}$  of the different porous PDMS samples with crosshatched geometries. The compressive modulus decreased with increasing filament spacing l, primarily because of filament spacing on the porosity  $\varphi$ . Thus, the mechanical properties of the porous structures were directly related to their porosity. In addition, the porous PDMS exhibited the highest compressive modulus when the filament angle was  $90^{\circ}$  (0/90). However, the corresponding staggered structure had the lowest compressive modulus (S-0/90). The ratios between the compressive moduli of these structures were 219, 411, and 686% for the l values of 0.6, 0.8, and 1.0 mm, respectively (Figure 3a–c). However, for the other cross-hatched structures with  $0^{\circ}/30^{\circ}$  and  $0^{\circ}/45^{\circ}$  filament angles, the compressive modulus remained in the same range.

The differences in the compressive modulus were closely related to the deformation mechanism in the initial linear elastic stage of these porous PDMS structures under compressive loading. To illustrate the compressive deformation mechanism of the porous structures fabricated by 3D printing with an l of 0.8 mm, the stress clouds of the x-zsection of the models were obtained, as shown in Figure 4. The compressive stresses of the 0/90-0.8 model in the z-direction were primarily transferred to a columnar pattern (yellow or green area in Figure 4c) along the intersection surface of contiguous filament layers from top to bottom [55]. The compressive stress in this region was obviously higher than that in the non-overlapping region for the PDMS model. Therefore, the compressive modulus of the 3D-printed PDMS with a 0°/90° layered pattern was primarily a result of the axial compressive deformation mechanism of these columns [55]. The corresponding staggered structure (Figure 4f) did not exhibit the stress column effect. Moreover, the upper layer of the filaments was squeezed, while the lower layer of the filaments experienced a bending deformation mechanism, resulting in a lower compressive modulus. For the other cross-hatched structures with 0°/30° and 0°/45° layered patterns (Figure 4a, b, d, and e),







**Figure 5:** Influence of layered staggering on the compressive behavior of the porous PDMS fabricated by 3D printing with filament raster angles of (a) 0°/30°, (b) 0°/45°, and (c) 0°/90°.

certain overlapping regions formed by adjacent layers of the filaments exhibited a stress column effect, resulting in compressive moduli being between those of 0/90-0.8 and S-0/90-0.8.

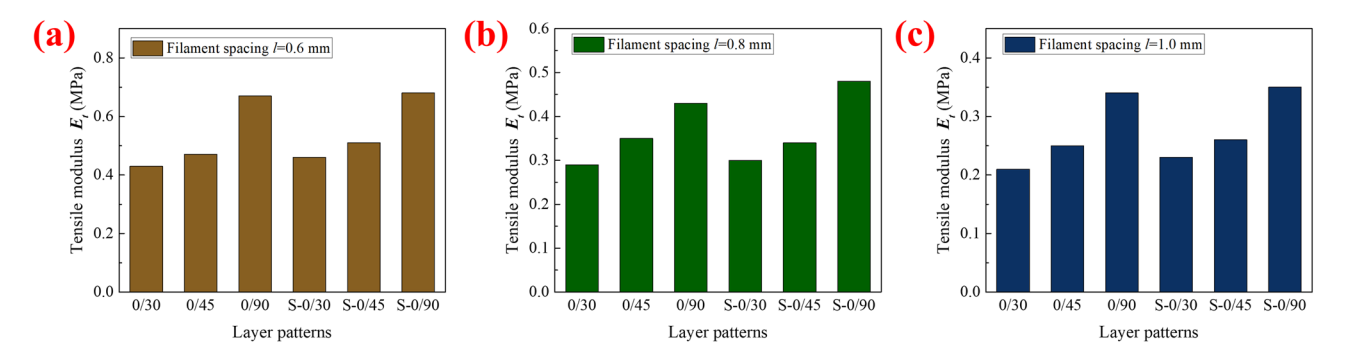


**Figure 6:** Influence of layer configurations on the  $E_t$  of the porous PDMS fabricated by 3D printing with filament spacings of (a) 0.6, (b) 0.8, and (c) 1.0 mm.

The compressive mechanical behavior of this 3D-printed PDMS was analogous to that of typical foams [55,57]. In the region of small and moderate deformation, the stress slowly increased, and the whole model completely entered the densified state, resulting in an exponential expansion of the compressive stress (Figure 5) [55,58]. In addition, the layered pattern had the same effect on the hyperelastic compressive behavior of the porous PDMS fabricated by 3D printing with the same porosity as that on  $E_c$ . For cross-hatched structures with 0°/30° and 0°/45° layered patterns, the compressive behavior of the porous PDMS fabricated by 3D printing with the same porosity was more consistent (Figure 5a and b), regardless of whether a staggered layer design was used or not. However, a significant difference was observed between the compressive behaviors of the 0/90 and S-0/90 models. The staggered design enabled the porous PDMS, with a layer angle of 0°/90° (S-0/90) to recover better (Figure 5c). Thus, it exhibited lower stress levels over a relatively long compression interval.

## 3.2 Effect of layered patterns on the tensile properties of 3D-printed PDMS

The uniaxial tensile simulation calculations of the porous PDMS fabricated by 3D printing with different cross-hatched structures were conducted using FE analysis. Figure 6 shows the y-axis tensile modulus ( $E_t$ ) of the porous PDMS fabricated by 3D printing with different values of l. The tensile modulus decreased with increasing l. This phenomenon was observed because the porosity of the PDMS sample increased with increasing l (Table 1). Consistent with the compression simulation results, the structure with the

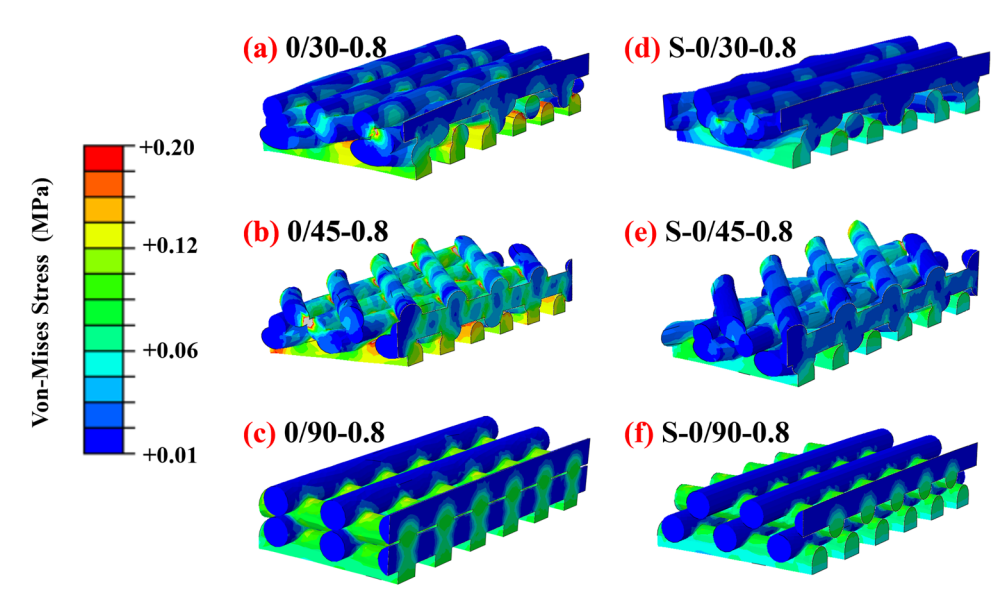


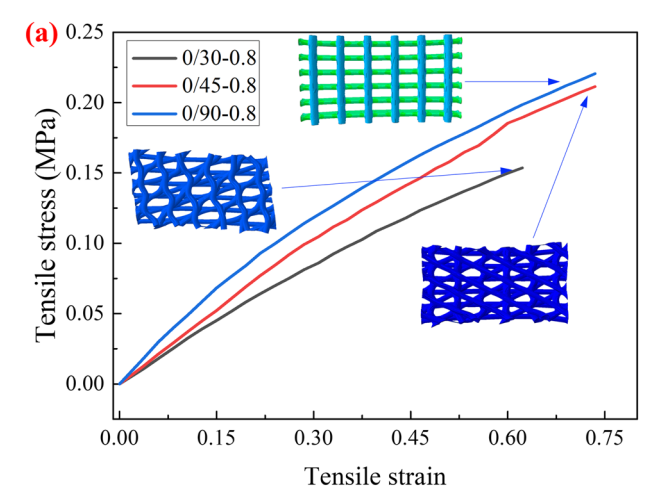
**Figure 7:** Von-Mises stress distributions of the models in the x–z section at 5% tensile strain in the y-direction: (a) 0/30-0.8, (b) 0/45-0.8, (c) 0/90-0.8, (d) S-0/30-0.8, (e) S-0/45-0.8, and (f) S-0/90-0.8.

S — Zhoukun He *et al.* DE GRUYTER

higher porosity exhibited a significantly lower tensile modulus than the other structures. In addition, the layered pattern regulated the tensile modulus of the porous PDMS fabricated by 3D printing with different porosities in a similar manner. As the filament angle increased (i.e., as the upper and lower layers of the adhesive filaments tended to orthogonality), their corresponding tensile moduli gradually increased. Furthermore, the porous PDMS with an l of 0.6 mm and a 0°/90° (0/90-0.6) layered pattern exhibited the highest tensile modulus, while the 3D-printed structures with 0°/30° and 0°/45° filament orientations exhibited reduced tensile moduli of 37 and 30%, respectively (Figure 6a). A similar change was observed for samples with filament spacing l of 0.8 and 1.0 mm printed with a 0°/90° (0/90-0.8 and 0/90-1.0) layered pattern, as shown in Figure 6b and c. However, the staggered layer design had no significant effect on the tensile moduli of these cross-hatched structures (S-0/30, S-0/45, and S-0/90), which remain in the same range as those of the 0/30, 0/45, and 0/90 models, respectively (Figure 6a-c).

The differences in the tensile modulus were closely related to the deformation mechanism in the initial linear elastic stage of these structures under tensile loading. To illustrate the tensile deformation mechanism of the 3Dprinted architectures at this stage, we obtained the Von-Mises stress clouds of the x–z sections of the models with a filament spacing of 0.8 mm (Figure 7). Because the direction of the filament layup was aligned with the tensile direction (y-axis), the stress in the 0/90-0.8 and S-0/90-0.8 models was primarily transferred in the filament orientation (green area in Figure 7c or f) [55]. The stress of this region was obviously higher than that of the porous PDMS fabricated by 3D printing with the 0°/30° and 0°/45° layered patterns (Figure 7a, b, d, and e). Thus, the tensile modulus of the porous PDMS fabricated by 3D printing with a crosshatched structure was due to the contribution of the axial tensile deformation mechanism of 3D-printed PDMS filaments. As the raster angle increased (i.e., the filament direction of these adjacent layers tended to orthogonality), the closer the filament orientation was to the tensile direction, the higher the tensile modulus of the corresponding porous PDMS fabricated by 3D printing. Therefore, the 3D-printed PDMS with a layer angle of 0°/90° exhibited the highest tensile modulus because the printing direction of the PDMS filament was parallel to the direction of the tensile load, which could bear more tensile stress. However, the staggered design (S-0/ 30, S-0/45, and S-0/90) did not change the raster angle for the corresponding porous architecture (0/30, 0/45, and 0/90), resulting in its inability to regulate the tensile properties of the porous PDMS fabricated by 3D printing.

The staggered design could not modulate the hyperelastic tensile mechanical behavior of the porous PDMS, and



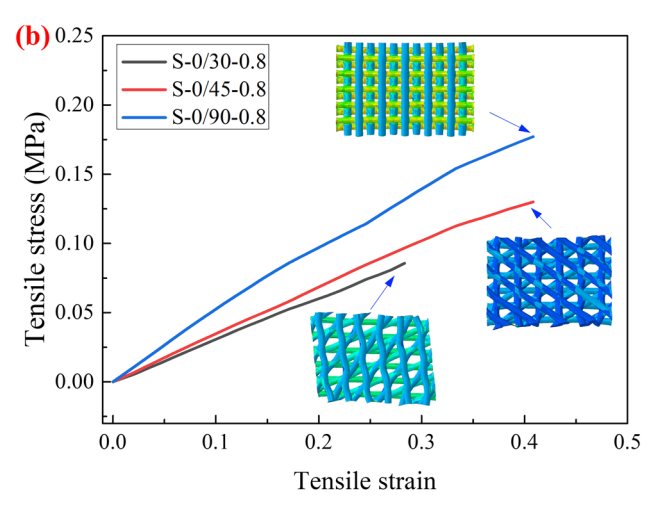


**Figure 8:** Influence of filament orientation on the tension behavior of the porous PDMS fabricated by 3D printing with (a) cross-hatched and (b) staggered structures.

a significant difference was observed between the tensile stresses of the FE models with different raster angles. As shown in Figure 8a and b, the tensile behaviors of the porous structures were better regulated by the layer angle of the filaments than by the staggered design. As the raster angle of the filaments increased (*i.e.*, the upper and lower filaments tended toward orthogonality), the tensile modulus gradually increased, and the tensile properties of the 3D-printed PDMS improved. The improved tensile stress was beneficial to both the mechanical stability of porous structures and superhydrophobicity.

#### 4 Conclusions

A strategy for the numerical simulation of the relationship between the layered pattern, such as filament angle and layer stagger, and mechanical behavior, such as tensile and compressive, of porous PDMS fabricated by 3D printing was presented. The results revealed that the compressive modulus decreased with increasing filament spacing. In addition, the staggered design could be used to modulate the compressive properties of the porous PDMS fabricated by 3D printing, which exhibited the highest compressive modulus when the filament angle was 90° (0/90). However, the corresponding staggered structure had the lowest compressive modulus (S-0/90). The ratios between the compressive moduli of the 0/90 and S-0/90 structures were 219, 411, and 686% for the filament spacing values of 0.6, 0.8, and 1.0 mm, respectively. However, the compressive properties of the porous PDMS fabricated by 3D printing with other filament angles (0°/30° and 0°/45°) were in the same range. The tensile modulus also decreased with increasing filament spacing, but the tensile behaviors of these 3D-printed structures were better regulated by the filament angle rather than the staggered design. With the increasing raster angle of the filaments (i.e., the upper and lower filaments tended to orthogonality), the tensile properties gradually improved. The porous PDMS fabricated by 3D printing with a filament spacing of 0.6 mm that was printed with a 0°/90° (0/90-0.6) layered pattern exhibited the highest tensile modulus, while the 3D-printed structures with 0°/30° and 0°/45° filament orientations exhibited reduced tensile moduli of 37 and 30%, respectively. A similar change was found for samples with filament spacings of 0.8 and 1.0 mm. Thus, the compressive and tensile properties of the 3D-printed PDMS with superhydrophobicity and a filament spacing of 0.8 could be regulated by adjusting the filament angle and staggered layer design. Because the superhydrophobicity of the 3D-printed PDMS was primarily controlled by the top-layer structures of the porous PDMS, the required layered pattern could be selected for the integrated design of mechanical and functional aspects in 3D-printed PDMS, considering the mechanical environment and the superhydrophobic properties.

Acknowledgments: The authors would like to acknowledge the financial support from the Sichuan Science and Technology Program (No. 2024NSFSC0246), the Natural Science Foundation of Henan (No. 232300420313), the National Natural Science Foundation of China (No. 51873240), the Key Research and Development Programs of Luzhou (No. 2022-GYF-12), the Talent Introduction Program of The Affiliated Stomatological Hospital of Southwest Medical University (No. 2022BS02), and the Innovative Leading Talents Program of The Affiliated Stomatological Hospital of Southwest Medical University (No. 2022LJ02).

Funding information: The authors acknowledge the financial support from the Sichuan Science and Technology Program (No. 2024NSFSC0246), the Natural Science Foundation of Henan (No. 232300420313), the National Natural Science Foundation of China (No. 51873240), the Key Research and Development Programs of Luzhou (No. 2022-GYF-12), the Talent Introduction Program of The Affiliated Stomatological Hospital of Southwest Medical University (No. 2022BS02), and the Innovative Leading Talents Program of The Affiliated Stomatological Hospital of Southwest Medical University (No. 2022LJ02).

Author contributions: Zhoukun He, Xiaowei Zhu, and Xiaorong Lan conceived and designed this study; Zhoukun He, Jie Su, Xiaowei Zhu, and Yue Li prepared the samples and wrote this paper; and Libo Yang, Xudong Zhang, Qi Jiang, and Xiaorong Lan made the finite element analysis and revised this paper. All authors have accepted responsibility for the entire content of this manuscript and approved its submission.

**Conflict of interest:** The authors state no conflict of interest.

Data availability statement: The datasets generated and/ or analyzed during the current study are available from the corresponding author on reasonable request.

#### References

- Park, J. H., B. S. Shin, and A. Jabbarzadeh. Anisotropic wettability on one-dimensional nanopatterned surfaces: The effects of intrinsic surface wettability and morphology. Langmuir, Vol. 37, 2021, pp. 14186-14194.
- Chen, D., Z. Mai, X. Liu, D. Ye, H. Zhang, X. Yin, et al. UV-blocking, [2] superhydrophobic and robust cotton fabrics fabricated using polyvinylsilsesquioxane and nano-TiO2. Cellulose, Vol. 25, 2018, pp. 3635-3647.
- Luo, X., G. Jiang, G. Wang, L. Yang, Y. He, K. Cui, et al. Novel approach to improve shale stability using super-amphiphobic nanoscale materials in water-based drilling fluids and its field application. Reviews on Advanced Materials Science, Vol. 61, 2022, pp. 41-54.
- [4] Liu, K. and L. Jiang. Bio-inspired design of multiscale structures for function integration. Nano Today, Vol. 6, 2011, pp. 155-175.
- Jiao, Z., Z. Wang, Z. Wang, and Z. Han. Multifunctional biomimetic composite coating with antireflection, self-cleaning and mechanical stability. Nanomaterials (Basel), Vol. 13, 2023, id. 1855.
- Yang, X., J. Song, W. Xu, X. Liu, Y. Lu, and Y. Wang. Anisotropic [6] sliding of multiple-level biomimetic rice-leaf surfaces on aluminium substrates. Micro & Nano Letters, Vol. 8, 2013, pp. 801-804.
- Wang, X., W. Song, Z. Li, and Q. Cong. Fabrication of superhydrophobic AAO-Ag multilayer mimicking dragonfly wings. Chinese Science Bulletin, Vol. 57, 2012, pp. 4635-4640.

- [8] Ju, J., Y. Zheng, and L. Jiang. Bioinspired one-dimensional materials for directional liquid transport. *Accounts of Chemical Research*, Vol. 47, 2014, pp. 2342–2352.
- [9] Cui, Y., D. Li, and H. Bai. Bioinspired smart materials for directional liquid transport. *Industrial & Engineering Chemistry Research*, Vol. 56, 2017, pp. 4887–4897.
- [10] Hong Tham Phan, T. and S.-J. Kim. Super-hydrophobic microfluidic channels fabricated via xurography-based polydimethylsiloxane (PDMS) micromolding. *Chemical Engineering Science*, Vol. 258, 2022, id. 117768.
- [11] Yu, L., Y. Xiong, L. Zou, Y. Zhao, S. Li, and S. Bi. Facile preparation of superhydrophobic and flame-retardant cotton fabrics. *Journal of Physics: Conference Series*, 2023, id. 2437.
- [12] Erdene-Ochir, O., V.-T. Do, and D.-M. Chun. Facile fabrication of durable and flexible superhydrophobic surface with polydimethylsiloxane and silica nanoparticle coating on a polyethylene terephthalate film by hot-roll lamination. *Polymer*, Vol. 255, 2022, id. 125158.
- [13] He, Z., M. Ma, X. Lan, F. Chen, K. Wang, H. Deng, et al. Fabrication of a transparent superamphiphobic coating with improved stability. *Soft Matter*, Vol. 7, 2011, pp. 6435–6443.
- [14] He, Z., M. Ma, X. Xu, J. Wang, F. Chen, H. Deng, et al. Fabrication of superhydrophobic coating via a facile and versatile method based on nanoparticle aggregates. *Applied Surface Science*, Vol. 258, 2012, pp. 2544–2550.
- [15] Chen, D., X. Hu, H. Zhang, X. Yin, and Y. Zhou. Preparation and properties of novel polydimethylsiloxane composites using polyvinylsilsesquioxanes as reinforcing agent. *Polymer Degradation and Stability*, Vol. 111, 2015, pp. 124–130.
- [16] Shinde, A., I. Siva, Y. Munde, I. Sankar, M. T. H. Sultan, F. S. Shahar, et al. Appraising the dielectric properties and the effectiveness of electromagnetic shielding of graphene reinforced silicone rubber nanocomposite. *Nanotechnology Reviews*, Vol. 12, 2023, id. 20220558.
- [17] Shan, Y., B. Tan, M. Zhang, X. Xie, and J. Liao. Restorative biode-gradable two-layered hybrid microneedles for melanoma photo-thermal/chemo co-therapy and wound healing. *Journal of Nanobiotechnology*, Vol. 20, 2022, id. 238.
- [18] Chen, D., W. Sun, C. Qian, A. P. Y. Wong, L. M. Reyes, and G. A. Ozin. UV-blocking photoluminescent silicon nanocrystal/polydimethylsiloxane composites. *Advanced Optical Materials*, Vol. 5, 2017, id. 1700237.
- [19] He, Z., N. Wang, X. Yang, L. Mu, Z. Wang, J. Su, et al. Antifouling induced by surface wettability of poly(dimethyl siloxane) and its nanocomposites. *Nanotechnology Reviews*, Vol. 12, 2023, id. 20220552.
- [20] He, Z., X. Yang, L. Mu, N. Wang, and X. Lan. A versatile "3M" methodology to obtain superhydrophobic PDMS-based materials for antifouling applications. *Frontiers in Bioengineering and Biotechnology*, Vol. 10, 2022, id. 998852.
- [21] Liao, X., X. Yu, H. Yu, J. Huang, B. Zhang, and J. Xiao. Development of an anti-infective coating on the surface of intraosseous implants responsive to enzymes and bacteria. *Journal of Nanobiotechnology*, Vol. 19, 2021, id. 241.
- [22] Vanithakumari, S. C., C. C. Johnson, and J. Philip. Facile fabrication of superhydrophobic steel surfaces with self-cleaning ability using nickel myristate/PDMS bilayer coating. Surface and Coatings Technology, Vol. 467, 2023, id. 129712.
- [23] Fan, L., B. Li, Y. Wang, J. He, J. Bai, T. Zhu, et al. Superhydrophobic epoxy/fluorosilicone/PTFE coatings prepared by one-step spraying

- for enhanced anti-icing performance. *Coatings*, Vol. 13, 2023, id. 569.
- [24] Zeng, Q., L. Kang, J. Fan, L. Song, S. Wan, B. Liao, et al. Durable superhydrophobic silica/epoxy resin coating for the enhanced corrosion protection of steel substrates in high salt and H2S environments. *Colloids and Surfaces, A: Physicochemical and Engineering Aspects*, Vol. 654, 2022, id. 130137.
- [25] Zheng, K., J. Zhu, H. Liu, X. Zhang, and E. Wang. Study on the superhydrophobic properties of an epoxy resin-hydrogenated silicone oil bulk material prepared by sol-gel methods. *Materials* (*Basel*), Vol. 14, 2021, id. 988.
- [26] Wang, J., Y. Zhang, and Q. He. Durable and robust superhydrophobic fluororubber surface fabricated by template method with exceptional thermostability and mechanical stability. *Separation* and Purification Technology, Vol. 306, 2023, id. 122423.
- [27] Hoshian, S., V. Jokinen, and S. Franssila. Robust hybrid elastomer/ metal-oxide superhydrophobic surfaces. *Soft Matter*, Vol. 12, 2016, pp. 6526–6535.
- [28] Wang, P., C. Li, and D. Zhang. Recent advances in chemical durability and mechanical stability of superhydrophobic materials: Multi-strategy design and strengthening. *Journal of Materials Science & Technology*, Vol. 129, 2022, pp. 40–69.
- [29] Morita, M., T. Koga, H. Otsuka, and A. Takahara. Macroscopic-wetting anisotropy on the line-patterned surface of fluoroalkylsi-lane monolayers. *Langmuir*, Vol. 21, 2005, pp. 911–918.
- [30] Bai, X., Q. Yang, H. Li, J. Huo, J. Liang, X. Hou, et al. Sunlight recovering the superhydrophobicity of a femtosecond laserstructured shape-memory polymer. *Langmuir*, Vol. 38, 2022, pp. 4645–4656.
- [31] He, Z., L. Mu, N. Wang, J. Su, Z. Wang, M. Luo, et al. Design, fabrication, and applications of bioinspired slippery surfaces. *Advances in Colloid and Interface Science*, Vol. 318, 2023, id. 102948.
- [32] He, Z., X. Lan, Q. Hu, H. Li, L. Li, and J. Mao. Antifouling strategies based on super-phobic polymer materials. *Progress in Organic Coatings*, Vol. 157, 2021, id. 106285.
- [33] He, Z., X. Yang, N. Wang, L. Mu, J. Pan, X. Lan, et al. Anti-biofouling polymers with special surface wettability for biomedical applications. *Frontiers in Bioengineering and Biotechnology*, Vol. 9, 2021, id. 807357.
- [34] Selim, M. S., H. Yang, S. A. El-Safty, N. A. Fatthallah, M. A. Shenashen, F. Q. Wang, et al. Superhydrophobic coating of silicone/β–MnO2 nanorod composite for marine antifouling. *Colloids and Surfaces, A: Physicochemical and Engineering Aspects*, Vol. 570, 2019, pp. 518–530.
- [35] Selim, M. S., A. Elmarakbi, A. M. Azzam, M. A. Shenashen, A. M. El-Saeed, and S. A. El-Safty. Eco-friendly design of superhydro-phobic nano-magnetite/silicone composites for marine foul-release paints. *Progress in Organic Coatings*, Vol. 116, 2018, pp. 21–34.
- [36] Xie, C., C. Li, Y. Xie, Z. Cao, S. Li, J. Zhao, et al. ZnO/acrylic polyurethane nanocomposite superhydrophobic coating on aluminum substrate obtained via spraying and Co-curing for the control of marine biofouling. *Surfaces and Interfaces*, Vol. 22, 2021, id. 100833.
- [37] He, W., J. Ou, F. Wang, S. Lei, X. Fang, W. Li, et al. Transparent and superhydrophobic coating via one-step spraying for cultural relic protection against water and moisture. *Colloids and Surfaces, A: Physicochemical and Engineering Aspects*, Vol. 662, 2023, id. 130949.
- [38] Wang, F., R. Ma, J. Zhan, T. Wang, and Y. Tian. Superhydrophobic starch-based cryogels modified with silylated magnetic

- nanoparticles for oil spill cleanup. Journal of Cleaner Production, Vol. 363, 2022, id. 132492.
- [39] Zhang, B., M. Qiao, G. Ji, and B. Hou. Durable corrosion resistant and hot water repellent superhydrophobic bilayer coating based on fluorine-free chemicals. Journal of Industrial and Engineering Chemistry, Vol. 119, 2023, pp. 346-356.
- [40] Song, J., H. Liu, M. Wan, Y. Zhu, and L. Jiang. Bio-inspired isotropic and anisotropic wettability on a Janus free-standing polypyrrole film fabricated by interfacial electro-polymerization. Journal of Materials Chemistry A, Vol. 1, 2013, pp. 1740-1744.
- [41] Cheng, L., Q. Xu, X. Jia, R. Zhang, S. Bai, Y. Qin, et al. Anisotropic wetting properties of oblique nanowires array and their applications on water transportation and fog collection. Surfaces and Interfaces, Vol. 22, 2021, id. 100784.
- [42] Li, L., Z. Xu, W. Sun, J. Chen, C. Dai, B. Yan, et al. Bio-inspired membrane with adaptable wettability for smart oil/water separation. Journal of Membrane Science, Vol. 598, 2020, id. 117661.
- [43] Hu, W., P. Zhang, X. Liu, B. Yan, L. Xiang, J. Zhang, et al. An amphiphobic graphene-based hydrogel as oil-water separator and oil fence material. Chemical Engineering Journal, Vol. 353, 2018, pp. 708-716.
- [44] Mai, Z., X. Shu, G. Li, D. Chen, M. Liu, W. Xu, et al. One-step fabrication of flexible, durable and fluorine-free superhydrophobic cotton fabrics for efficient oil/water separation. Cellulose, Vol. 26, 2019, pp. 6349-6363.
- [45] Li, Z., A. Zheng, Z. Mao, F. Li, T. Su, L. Cao, et al. Silk fibroin-gelatin photo-crosslinked 3D-bioprinted hydrogel with MOF-methylene blue nanoparticles for infected wound healing. International Journal of Bioprinting, Vol. 9, 2023, id. 773.
- [46] Li, C., J. Wang, W. Yang, K. Yu, J. Hong, X. Ji, et al. 3D-printed hydrogel particles containing PRP laden with TDSCs promote tendon repair in a rat model of tendinopathy. Journal of Nanobiotechnology, Vol. 21, 2023, id. 177.
- [47] Jafari, A., S. Vahid Niknezhad, M. Kaviani, W. Saleh, N. Wong, P. P. Van Vliet, et al. Formulation and evaluation of PVA/gelatin/carrageenan inks for 3D printing and development of tissue-engineered heart valves. Advanced Functional Materials, Vol. 34, 2024,
- [48] Menasce, S., R. Libanori, F. B. Coulter, and A. R. Studart. 3D-printed architectured silicones with autonomic self-healing and creep-resistant behavior. Advanced Materials, Vol. 36, 2024, id. 2306494.
- [49] Riester, O., S. Laufer, and H.-P. Deigner. Direct 3D printed biocompatible microfluidics: Assessment of human mesenchymal stem cell differentiation and cytotoxic drug screening in a dynamic culture system. Journal of Nanobiotechnology, Vol. 20, 2022, id. 540.
- [50] Alioglu, M. A., Y. O. Yilmaz, E. M. Gerhard, V. Pal, D. Gupta, S. H. A. Rizvi, et al. A versatile photocrosslinkable silicone composite for 3D

- printing applications. Advanced Materials Technologies, Vol. 9, 2024, id. 2301858.
- [51] Dang, W., W.-C. Chen, E. Ju, Y. Xu, K. Li, H. Wang, et al. 3D printed hydrogel scaffolds combining glutathione depletion-induced ferroptosis and photothermia-augmented chemodynamic therapy for efficiently inhibiting postoperative tumor recurrence. Journal of Nanobiotechnology, Vol. 20, 2022, id. 266.
- Marovič, N., I. Ban, U. Mayer, and T. Mayer, Magnetic nanoparticles [52] in 3D-printed scaffolds for biomedical applications. Nanotechnology Reviews, Vol. 12, 2023, id. 20220570.
- [53] He, Z., Y. Chen, J. Yang, C. Tang, J. Lv, Y. Liu, et al. Fabrication of polydimethylsiloxane films with special surface wettability by 3D printing. Composites, Part B: Engineering, Vol. 129, 2017, pp. 58-65.
- [54] He, Z., N. Wang, L. Mu, Z. Wang, J. Su, Y. Chen, et al. Porous polydimethylsiloxane films with specific surface wettability but distinct regular physical structures fabricated by 3D printing. Frontiers in Bioengineering and Biotechnology, Vol. 11, 2023, id. 1272565.
- [55] Zhu, X., Y. Li, Y. Shi, L. Hou, G. Wang, Z. He, et al. Structure-mechanical property relationships of 3D-printed porous polydimethylsiloxane films. Nanotechnology Reviews, Vol. 12, 2023, id. 20230188.
- Zhu, X., Y. Shi, F. Sun, F. Hou, Y. Li, J. Wen, et al. Stress relaxation [56] behavior of 3D printed silicone rubber foams with different topologies under uniaxial compressive load. Composites Communications, Vol. 38, 2023, id. 101475.
- Zhu, X., Y. Chen, Y. Liu, Y. Deng, C. Tang, W. Gao, et al. Additive **[57]** manufacturing of elastomeric foam with cell unit design for broadening compressive stress plateau. Rapid Prototyping Journal, Vol. 24, 2018, pp. 1579-1585.
- [58] Gibson, L. J. Cellular solids: Structure and properties, 2nd ed., Cambridge University Press, Cambridge, 2003.
- Ammar, S., B. Ben Fraj, H. Hentati, A. Saouab, M. Ben Amar, and M. Haddar. Mechanical performances of printed carbon fiberreinforced PLA and PETG composites. Proceedings of the Institution of Mechanical Engineers, Part L: Journal of Materials: Design and Applications, Vol. 238, 2024, pp. 1488-1499.
- Allouch, M., B. Ben Fraj, M. Dhouioui, A. Kesssentini, H. Hentati, M. Wali, et al. Mechanical, microstructural and numerical investigations of 3D printed carbon fiber reinforced PEEK. Proceedings of the Institution of Mechanical Engineers, Part C: Journal of Mechanical Engineering Science, Vol. 238, 2023, pp. 2131-2139.
- [61] Moroni, L., J. R. de Wijn, and C. A. van Blitterswijk. 3D fiberdeposited scaffolds for tissue engineering: Influence of pores geometry and architecture on dynamic mechanical properties. Biomaterials, Vol. 27, 2006, pp. 974-985.
- Treloar, L. R. G. The physics of rubber elasticity, Oxford University Press, Oxford, 2005.